

Northumbria Research Link

Citation: Ren, Xiaohe, Gan, Ziwei, Sun, Mengxuan, Fang, Qisheng, Yan, Yijun, Sun, Yongxiu, Huang, Jianan, Cao, Baobao, Shen, Wenzhong, Li, Zhijie and Fu, Yong Qing (2022) Colloidal synthesis of flower-like Zn doped Ni(OH)₂@CNTs at room-temperature for hybrid supercapacitor with high rate capability and energy density. *Electrochimica Acta*, 414. ISSN 0013-4686

Published by: Elsevier

URL: <https://doi.org/10.1016/j.electacta.2022.140208>
<<https://doi.org/10.1016/j.electacta.2022.140208>>

This version was downloaded from Northumbria Research Link:
<https://nrl.northumbria.ac.uk/id/eprint/48663/>

Northumbria University has developed Northumbria Research Link (NRL) to enable users to access the University's research output. Copyright © and moral rights for items on NRL are retained by the individual author(s) and/or other copyright owners. Single copies of full items can be reproduced, displayed or performed, and given to third parties in any format or medium for personal research or study, educational, or not-for-profit purposes without prior permission or charge, provided the authors, title and full bibliographic details are given, as well as a hyperlink and/or URL to the original metadata page. The content must not be changed in any way. Full items must not be sold commercially in any format or medium without formal permission of the copyright holder. The full policy is available online: <http://nrl.northumbria.ac.uk/policies.html>

This document may differ from the final, published version of the research and has been made available online in accordance with publisher policies. To read and/or cite from the published version of the research, please visit the publisher's website (a subscription may be required.)

1 **Colloidal synthesis of flower-like Zn doped**
2 **Ni(OH)₂@CNTs at room-temperature for**
3 **hybrid supercapacitor with high rate**
4 **capability and energy density**

5 Xiaohu Ren^a, Ziwei Gan^a, Mengxuan Sun^a, Qisheng Fang^a, Yijun Yan^a, Yongxiu Sun^a,
6 Jianan Huang^b, Baobao Cao^b, Wenzhong Shen^c, Zhijie Li^{a,*}, Yongqing Fu^{d,*}

7
8 ^a School of Physics, University of Electronic Science and Technology of China,
9 Chengdu, 6111731, P. R. China

10 ^b Key Laboratory of Advanced Technologies of Materials, Ministry of Education,
11 Southwest Jiaotong University, Chengdu 610031, PR China

12 ^c State Key Laboratory of Coal Conversion, Institute of Coal Chemistry, Chinese
13 Academy of Science, Taiyuan, 030001, P. R. China

14 ^d Faculty of Engineering and Environment, Northumbria University, Newcastle Upon
15 Tyne, NE1 8ST, UK

16
17
18
19 Zhijie Li (**Corresponding Author**): ORCID: 0000-0001-9870-9939;

20 *E-mail: zhijieli@uestc.edu.cn; TEL: +86 02883202160

21 Yongqing (Richard) Fu (**Corresponding Author**): ORCID: 0000-0001-9797-4036;

22 *E-mail: Richard.fu@northumbria.ac.uk; TEL: +44 (0)191 2274662

1 **Abstract**

2 Transition metal oxides and hydroxides are typically applied as electrode materials
3 for supercapacitors, but it is often difficult to achieve both their high power density
4 and energy density simultaneously. Herein, electrodes of flower-like Zn doped
5 Ni(OH)₂ combined with carbon nanotubes (i.e., Zn doped Ni(OH)₂@CNTs) were *in-*
6 *situ* synthesized using a colloidal synthesis method at room-temperature, assisted by
7 cetyltrimethyl ammonium bromide (CTAB) and NaBH₄. This electrode exhibits an
8 excellent electrochemical performance, achieving a high specific capacity of 750.5 C
9 g⁻¹ at 0.5 A g⁻¹ and maintaining 72.9% of its initial value when the current density is
10 increased from 1 A g⁻¹ to 10 A g⁻¹. A hybrid supercapacitor (HSC) assembled using the
11 Zn doped Ni(OH)₂@CNTs as the positive electrode and an active carbon as the
12 negative electrode exhibits a capacity of 201.7 C g⁻¹ at 1 A g⁻¹ and an energy density
13 of 51.3 Wh kg⁻¹ at a power density of 409.6 W kg⁻¹. After running for 50,000 cycles at
14 a current density of 6 A g⁻¹, the capacity of the HSC becomes 115.8% of its initial
15 value. Moreover, this HSC maintains a high energy density of 29.33 Wh kg⁻¹ at a high
16 power density of 16.5 kW kg⁻¹ after cycling for 50,000 times, which indicates its
17 suitability for energy storage applications.

18 **Key words:** Ni(OH)₂, CNTs, Colloidal method, Supercapacitors, Rate capability

1

2 **1 Introduction**

3 Due to the reduced production of fossil fuels and severe environmental pollution,
4 people are trying to search for green, efficient and environment-friendly energy storage
5 technologies [1]. Among them, supercapacitors (SCs) receive substantial attention
6 owing to their low-cost, short charging time, prominent power density, long cyclic life
7 and environmental friendliness [2, 3]. Furthermore, hybrid supercapacitors (HSCs) [4],
8 which combine battery-type and capacitive-type electrodes, exhibit a better
9 electrochemical performance compared with the conventionally asymmetric
10 supercapacitors (ASCs), and can also achieve a higher energy density. Therefore, it has
11 been a hot topic to explore new electrode materials for the HSCs.

12 Transition metal oxides (TMO) or hydroxides (TMH) have attracted significant
13 attention as the battery-type electrode materials. Among these, Ni(OH)₂ has been
14 studied extensively due to its low-cost and a high theoretical capacity of 2082.0 F g⁻¹,
15 which makes Ni(OH)₂ an ideal electrode material for HSCs [5-7]. However, there are
16 various issues of Ni(OH)₂ based electrodes such as poor electrical conductivity and rate
17 capability. One of the effective strategies to improve the electrochemical performance
18 of these electrode materials is to change their morphologies, for examples, the Ni(OH)₂
19 based materials can be synthesized into various structures and morphologies, including
20 flower-like [8], nanorods [9], nanoparticles [10] and microspheres [11]. However, these
21 special morphologies are generally synthesized by growing directly on the substrates
22 of collectors, or using a template method. For example, flower-like Ni(OH)₂ was grown

1 directly onto graphene via a microwave heating method, and the obtained electrode
2 showed a large specific capacitance of 1735.0 F g^{-1} at a scan rate of 1 mV s^{-1} , with a
3 rate capability of 30% at 50 mV s^{-1} [12]. Microspheres of $\alpha\text{-Ni(OH)}_2$ were grown via
4 a solvothermal method and then made into an electrode, which achieved a specific
5 capacitance of 1087.1 F g^{-1} at 1 A g^{-1} , with a rate capability of 54.7% at 10 A g^{-1} [11].
6 Flower-like microspheres of Zn-doped Ni-based metal-organic frameworks (MOFs)
7 were synthesized using a hydrothermal method, and the corresponding electrode
8 displayed a high specific capacitance of 1620.0 F g^{-1} at 0.25 A g^{-1} [13]. Among these
9 various structures, flower-like one can shorten the diffusion paths of ions, provide more
10 active sites for full contacts with the electrolyte, and achieve a high capacity. However,
11 its poor rate capability and stability need to be improved.

12 Addition of heterogeneous elements such as Co [14], Mo [15], Cu [16], Zn [17] and
13 Mn [18] into the electrodes can further improve the electrochemical performance of the
14 HSCs. Among these heterogeneous elements, Zn has attracted much attention due to its
15 low-cost, wide availability and large concentration of holes if replacing the other metal-
16 ions [19]. Moreover, adding a proper amount of Zn element can accelerate the electron
17 transfer, and improve the electrochemical activity and stability of TMHs [20]. For
18 examples, Wu et al. prepared ultrathin ZnNi layered double hydroxide nanosheets
19 through a zeolitic imidazolate frameworks-8 derived approach, which achieved a high
20 capacitance of $3967.0 \text{ mF cm}^{-2}$ at 2.0 mA cm^{-2} [21]. Ni-Zn-Fe layered mesoporous
21 double hydroxide was prepared by a method combining ionic layer adsorption and
22 reaction [22]. The electrode made of this double hydroxide achieved a good specific

1 capacitance of 1452.3 F g^{-1} at a scan rate of 5 mV s^{-1} and the assembled HSC achieved
2 an energy density of 14.9 Wh kg^{-1} at a power density of 1.07 kW kg^{-1} [22]. Although
3 addition of Zn element has greatly improved the specific capacity, but the value is still
4 far too low for the practical applications which demand both high energy density and
5 high power density.

6 In this work, with the help of cetyltrimethyl ammonium bromide (CTAB) and sodium
7 borohydride (NaBH_4), a flower-like Zn doped $\text{Ni}(\text{OH})_2$ electrode material was *in-situ*
8 synthesized using a colloidal method at room temperature. Meanwhile, CNTs with their
9 tubular and porous structures were further integrated into the above electrode material,
10 and improve the electrical conductivity of the electrode [23, 24]. The electrode was
11 prepared by coating flower-like nanomaterials on a nickel foam, which showed large
12 specific capacity and good rate capability. Furthermore, the Zn doped
13 $\text{Ni}(\text{OH})_2@\text{CNTs}/\text{AC}$ HSC achieved a high energy density of 51.3 Wh kg^{-1} at the power
14 density of 409.6 W kg^{-1} and a remarkable long-term stability.

15

16 **2 Experimental details**

17 ***2.1 Preparation of ZNC nanosheets***

18 Chemicals information for this work is provided in the supplementary information.
19 In a typical experiment, 0.130 g of $\text{Zn}(\text{CH}_3\text{COO})_2 \cdot 2\text{H}_2\text{O}$, 0.590 g of
20 $\text{Ni}(\text{CH}_3\text{COO})_2 \cdot 4\text{H}_2\text{O}$ and 1.800 g CTAB were successively added into a beaker of 80
21 ml in volume, with deionized (DI) water. The solution was stirred for 10 min at room
22 temperature of 25°C , and marked as Solution A. 50 mg CNTs were ultrasonically

1 dispersed into 20 ml DI water for 30 min. Then the formed CNTs solution was added
2 into Solution A and stirred for another 10 min until the mixed solution became
3 homogeneous. This solution was labelled as Solution B. NaBH₄ of 0.378 g was
4 dissolved in 5 ml DI water and added into Solution B. Many bubbles were formed, and
5 the solution was stirred until the bubbles were disappeared. The formed black
6 precipitate was then collected, and cleaned three times with a mixed solution of DI
7 water and ethanol. Finally, the black precipitate was dried at 60 °C for 12 h to obtain
8 the ZNC-8.4% sample. For this sample, the molar ratio of Zn and Ni is 1:3.8, and the
9 mass of CNTs was 8.4%. To study the effect of different mass ratios of CNTs, CNTs of
10 0, 20 and 80 mg were added into the solution using the same synthetic process, and the
11 obtained samples were named as ZN, ZNC-5.6% and ZNC-14.6%, respectively.

12 ***2.2 Physical characterization***

13 Crystalline structure of the material was analyzed using an X-ray diffractometer
14 (XRD, Cu K α , Rigaku D/max-2400). Morphology of the material was observed using
15 a scanning electron microscope (SEM, Inspect F50) and its internal microstructure was
16 characterized using a transmission electron microscope (TEM, JEM-2200FS, Japan).
17 Chemical states of elements were characterized using an X-ray photoelectron
18 spectroscopy (XPS, Al K α radiation, ESCALAB 250Xi). Specific surface area of Zn
19 doped Ni(OH)₂@CNTs was characterized using a N₂ physisorption apparatus (JW-
20 BK122W, JWGB SCI. TECH.), and was determined using the Brunauer-Emmett-Teller
21 (BET) theory. Barrett-Joyner-Halenda (BJH) method was used to calculate the
22 volume and size distribution of pores.

1 **2.3 Electrochemical characterizations**

2 The prepared active electrodes and HSC devices are summarized in the
3 supplementary information. For the three-electrode testing system, the synthesized
4 active electrode, platinum foil electrode and Hg/HgO electrode were used as the
5 working electrode, counter electrode and reference electrode, respectively. All the
6 cyclic voltammetry (CV), galvanostatic charge-discharge (GCD) and electrochemical
7 impedance spectroscopy (EIS) were tested in a 2 M KOH electrolyte solution.

8 The specific capacity C_s ($C\ g^{-1}$) of working electrode can be calculated according to
9 the following formula [25]:

$$10 \quad C_s = \frac{I \times \Delta t}{m} \quad (1)$$

11 where I , Δt and m represent the discharge current (A), discharge time (s) and mass (g)
12 of the corresponding active electrode, respectively.

13 The specific capacity (C_{HSC} , $C\ g^{-1}$), energy density (E , $Wh\ kg^{-1}$), and power density (P ,
14 $W\ kg^{-1}$) of the HSC devices were calculated based on the total mass (M , g) of the two
15 electrodes using the following equations [27]:

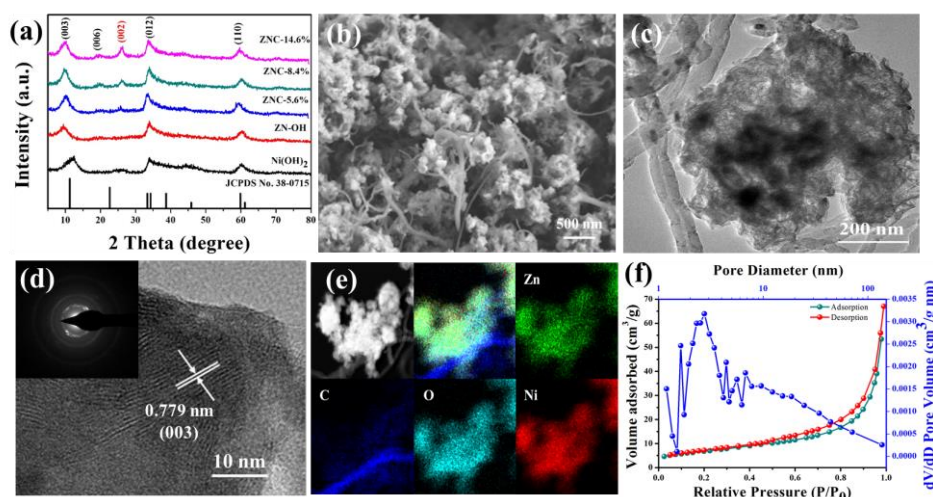
$$16 \quad C_{HSC} = \frac{I \times \Delta t}{M} \quad (2)$$

$$17 \quad E = \frac{C_{HSC} \times \Delta V}{2 \times 3.6} \quad (3)$$

$$18 \quad P = \frac{E \times 3600}{\Delta t} \quad (4)$$

19 **3 Results and discussion**

20 **3.1 Structure characterization of ZNC samples**



1

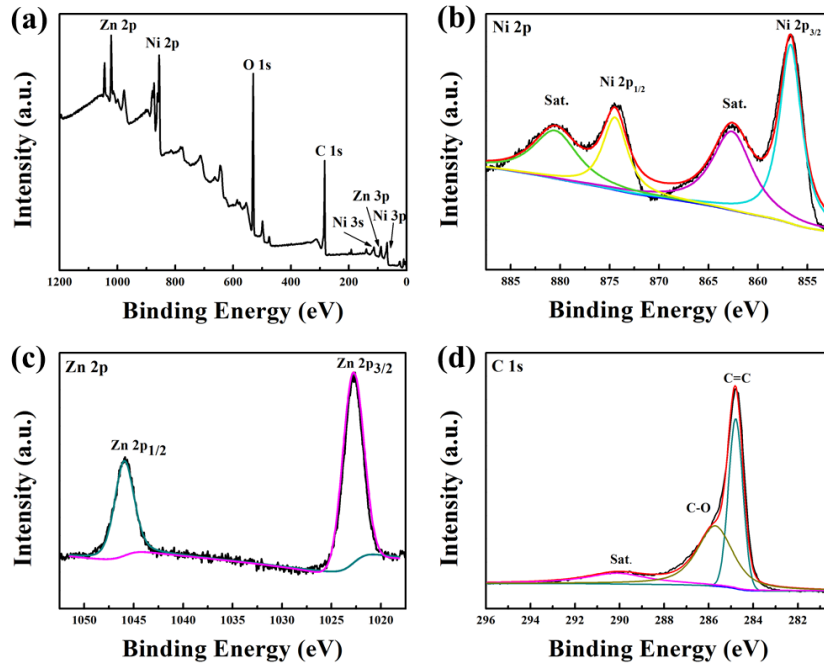
2 Fig. 1 (a) XRD spectra of Ni(OH)₂, ZN, ZNC-5.6%, ZNC-8.4% and ZNC-14.6%
 3 samples, (b) SEM, (c) TEM, (d) HR-TEM images (the inset is the corresponding
 4 SAED pattern) and (e) EDX elemental mapping of ZNC-8.4%, (f) N₂
 5 adsorption/desorption isotherms of ZNC-8.4% and the pore size distributions image.

6 Crystallographic structures of the synthesized ZNC samples were characterized
 7 using XRD and the obtained spectra are shown in Fig. 1a. The diffraction peaks of all
 8 the ZNC samples (located at 11.3°, 22.7°, 34.4° and 59.9°) are associated to the (003),
 9 (006), (012) and (110) planes of the α -Ni(OH)₂·0.75H₂O (JCPDS No. 38-0715) [20,
 10 28-30]. This indicates that the structure of Ni(OH)₂·0.75H₂O has not been changed
 11 obviously after doped by Zn ions. Compared with that of α -Ni(OH)₂, the (003)
 12 diffraction peaks of ZNC are shifted to the lower two theta angle, suggesting that the
 13 lattice spacing of the crystals are increased after doped with Zn ions [13, 31]. The
 14 expansion of the (003) crystal planes indicates that more ions can be accommodated to
 15 promote the rapid transfer of electrons [18]. Based on the Scherrer equation [25], the
 16 average diameter of active material can be estimated as ~3.6 nm. In addition, there is a
 17 diffraction peak at ~26.0°, which is corresponding to the (002) crystal plane of CNTs

1 (JCPDS, 65-6212) [32, 33].

2 Figs. 1b and 1c display SEM and TEM images of the ZNC-8.4%. Flower-like
3 structures can be observed and are composed of nanosheets and CNTs, which are
4 uniformly dispersed inside the sample. Fig. 1d shows the HR-TEM image, in which the
5 lattice fringes of 0.779 nm match well with the (003) plane of $\alpha\text{-Ni(OH)}_2\cdot 0.75\text{H}_2\text{O}$.
6 Selected area electron diffraction (SAED) pattern shown in inset of Fig. 1d reveals the
7 polycrystalline nature of the ZNC-8.4% nanosheets. EDX elemental mapping results of
8 ZNC-8.4% are shown in Fig.1e, which proves the elements of Zn, Ni and O are
9 uniformly distributed and the CNTs are uniformly embedded within the sample.

10 Fig. 1f shows the N_2 adsorption/desorption isotherms of ZNC-8.4% and the pore size
11 distributions. The obtained curve of N_2 adsorption/desorption isotherms shows a type-
12 IV isotherm and a hysteresis loops [34], demonstrating the existence of mesoporous
13 structure in the flower-like ZNC-8.4%. The pore sizes distribution (PSD) are ranged
14 from 1.5 nm to 100 nm but mainly centered at ~ 3 nm with a large pore volume of 0.104
15 $\text{cm}^3 \text{g}^{-1}$ (see the blue curve). The surface area was calculated based on the N_2 adsorption
16 isotherms, and the BET surface area was estimated to be $28.354 \text{ m}^2 \text{g}^{-1}$. The sample has
17 a uniquely mesoporous structure and a high specific surface area, which can effectively
18 shorten the ion transport paths and promote the faradic reactions in the charge and
19 discharge processes.



1
 2 Fig. 2 (a) XPS survey spectrum of the ZNC-8.4%. High-resolution XPS spectra of (b)
 3 Ni 2p; (c) Zn 2p; (d) C 1s.

4 Chemical states and elemental compositions of ZNC-8.4% sample were
 5 characterized by XPS analysis. The survey spectrum shown in Fig. 2a proves the
 6 existence of the elements of Ni, Zn, O and C in ZNC-8.4% sample. For the high
 7 resolution XPS spectra of Ni 2p shown in Fig. 2b, two peaks around 856.7 and 874.4
 8 eV are corresponding to the Ni 2p_{3/2} and Ni 2p_{1/2} levels, respectively, suggesting the
 9 presence of Ni²⁺ [35, 36]. While the other two peaks at 862.6 and 880.5 eV are the
 10 satellite peaks. The two peaks at 1022.8 and 1045.9 eV in Fig. 2c are attributed to Zn
 11 2p_{3/2} and Zn 2p_{1/2}, suggesting the presence of Zn²⁺ and confirming the doped Zn
 12 samples [37]. Fig. 2d shows high-resolution C 1s spectrum, in which two peaks at 284.7
 13 and 285.7 eV are attributed to the C=C groups in the CNTs and C-O groups on the
 14 surfaces of CNTs [38], respectively.

3.2 Electrochemical properties of ZNC-8.4% sample

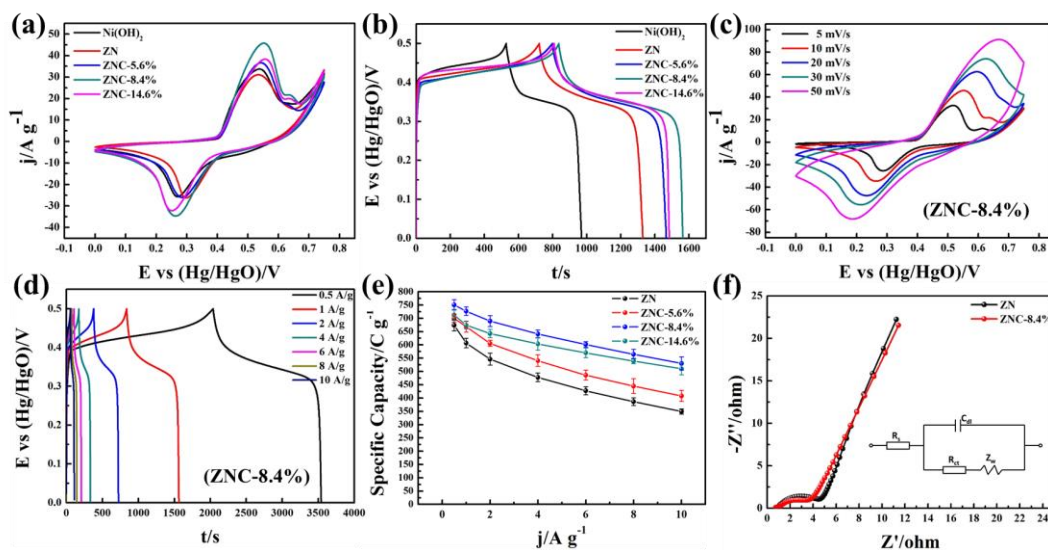


Fig. 3 (a) CV curves at the scan rate of 10 mV s^{-1} and (b) GCD curves from 0 to 0.5 V at the current density of 1 A g^{-1} of $\text{Ni}(\text{OH})_2$, ZN, ZNC-5.6%, ZNC-8.4% and ZNC-14.6% samples, (c) CV curves at different scan rates, and (d) GCD curves from 0 to 0.5 V at different current densities of ZNC-8.4%, (e) specific capacities of ZN, ZNC-5.6%, ZNC-8.4% and ZNC-14.6% samples at different current densities, and (f) Nyquist plots of ZN and ZNC-8.4% samples at the potential of 0.358 V (inset is the corresponding equivalent circuit). (Three-electrode testing system was used with 2 M KOH electrolyte and the sample loading of 2.1 mg)

We have changed different mole ratios of Zn and Ni, and studied electrochemical performance of the synthesized ZNC samples. When the mole ratio of Zn and Ni is 1:4, the specific capacity can reach the maximum value of 606.8 C g^{-1} at a current density of 1 A g^{-1} , as shown in Fig. S1. However, the rate capacity is quite low (57.5% with the current density from 1 A g^{-1} to 10 A g^{-1}). It is noted that adding appropriate CNTs can enhance its rate capacity.

1 In order to optimize the percentage of CNTs, CV and GCD curves of α -
2 $\text{Ni}(\text{OH})_2 \cdot 0.75\text{H}_2\text{O}$, ZN and ZNC electrodes were obtained and investigated. Fig. 3a and
3 Fig. S2 show the CV curves and the repeat results obtained in a 2 M KOH aqueous
4 electrolyte at 10 mV s^{-1} with a potential range of 0~0.75 V, and the Fig. 3b shows the
5 GCD curves tested at a current density of 1 A g^{-1} . All the CV curves show a pair of
6 redox peaks with an obvious separation between them. There is also an obviously large
7 potential plateau in all the GCD curves during the charging and discharging processes,
8 suggesting the battery-type characteristics of ZNC electrode materials. The loop areas
9 of these CV curves for the ZNC electrode material are obviously larger than those of
10 the ZN electrode materials. According to the discharge time of GCD curve, the addition
11 of CNTs is beneficial for the improvement of capacity. Furthermore, the CV and GCD
12 curves of ZNC electrode show the largest capacity value with the content of CNTs of
13 8.4%.

14 As the ZNC-8.4% electrode has the largest capacity than the other compounds, its
15 electrochemical performance was further investigated in details. Fig. 3c shows the CV
16 curves of ZNC-8.4% at different scanning rates from 5 to 50 mV s^{-1} . Their similar
17 shapes indicate a good reversibility in the charging and discharging processes.
18 Moreover, their redox peaks are shifted toward both sides of positive and negative
19 voltages with the increase of scanning rate. This is mainly due to the increase of
20 electrode polarization at higher scanning rates and the increased internal resistance of
21 the electrodes [39, 40]. The redox peaks are mainly dependent on the reaction of
22 $\text{Ni}(\text{OH})_2$ [41], based on the following equation (5):



2 Meanwhile, we also studied the reaction mechanism of active materials by fitting $\log i$ -
3 $\log \nu$ curve, according to formula (6) [42]:

4
$$i = a\nu^b \quad (6)$$

5 where i (A) is the redox peak current, ν (mV s^{-1}) is scan rate from the CV curves in Fig.
6 3c, a and b are adjustable parameters. The energy storage behavior of the active
7 materials can be assessed by calculating the value of b (e.g., the fitted slope of the curve).
8 When the b value is 0.5, the electrode material behaves as a diffusion-controlled battery
9 type, whereas when the b value is 1, it behaves as a surface-controlled capacitive type
10 [27]. As shown in Fig. S4, the b value of the ZNC-8.4% is 0.44, which indicates that
11 the energy storage type is the battery-type, and the energy storage mechanism is mainly
12 the diffusion-controlled one.

13 Fig. 3d shows the GCD curves of ZNC-8.4% at various current densities of 0.5~10
14 A g^{-1} with a potential window of 0~0.5 V. Due to the faradaic redox reaction between
15 Ni(OH)_2 and electrolyte [43], the potential plateaus can be clearly seen in the charge-
16 discharge process of all GCD curves. Moreover, the symmetry of GCD curves shows
17 that the electrode material has a good coulomb efficiency in the charging and
18 discharging processes.

19 The specific capacity of electrode can be obtained using the GCD curves according
20 to formula (1). As shown in Fig 3e, the ZNC-8.4% electrode has the best
21 electrochemical performance, and its specific capacity values are 750.5, 726.5, 689.2,
22 641.2, 601.2, 564.8 and 530.0 C g^{-1} at different current densities of 0.5, 1, 2, 4, 6, 8 and

1 10 A g⁻¹, respectively. Furthermore, the capacity of the ZNC-8.4% electrode can
 2 maintain 72.9% from 1 to 10 A g⁻¹, which is much higher than that of the ZN electrode
 3 (which is 57.5%). Therefore, we can confirm that the CNTs can be used to improve its
 4 rate capacity. In addition, the DC conductivity of ZNC samples at different CNT
 5 loadings were tested, and the conductivity was increased with the increase of CNT
 6 loadings (see in Fig. S3).

7 Table 1 lists electrochemical properties of the reported nickel oxide based electrodes
 8 in literature, along with the data obtained from this study. The specific capacity and rate
 9 performance of ZN electrode have been improved effectively by the addition of CNTs.
 10 As listed in Table 1, the ZNC-8.4% composite exhibits higher capacity and better rate
 11 performance than those of other nickel oxide based electrode materials reported in
 12 literature.

13 Table 1. Comparisons of electrochemical properties of ZNC-8.4% with the reported
 14 nickel oxide based electrode materials

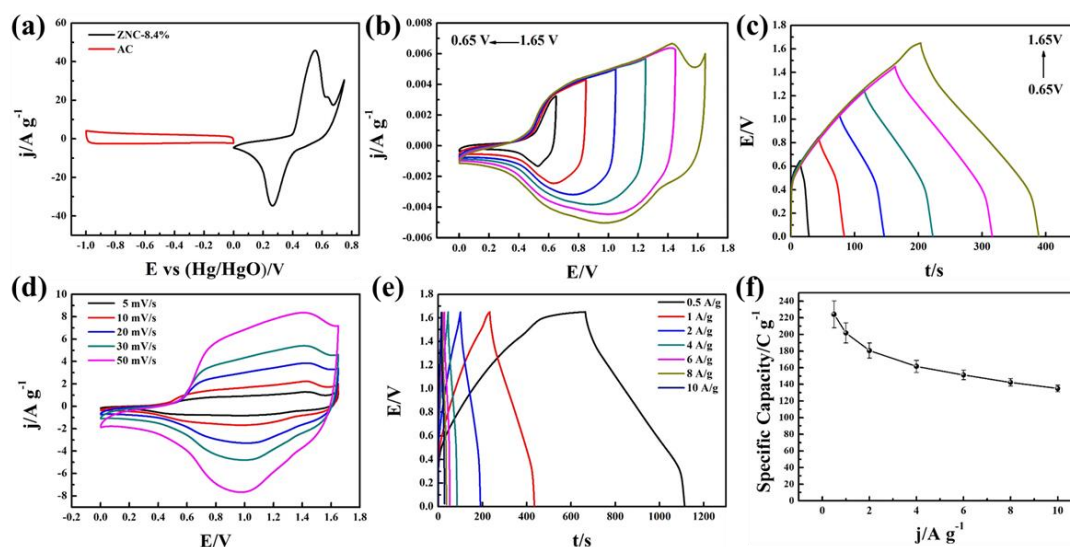
Materials	Method	Capacity	Rate Capacity	Ref.
Ni(OH) ₂ /nitrogen-doped GO	hydrothermal	896.0 F g ⁻¹ at 0.5 A g ⁻¹	56.2% at 12 A g ⁻¹	[44]
Zn doped Ni-based MOFs	solvothermal	298.0 C g ⁻¹ at 0.5 A g ⁻¹	34.8% at 10 A g ⁻¹	[45]
NiO@Ni(OH) ₂ -α-MoO ₃	hydrothermal	445.0 F g ⁻¹ at 1 A g ⁻¹	8.3% at 5 A g ⁻¹	[15]
Ni-Zn/rGO	hydrothermal	615.4 C g ⁻¹ at 1 A g ⁻¹	62.3% at 30 A g ⁻¹	[20]
ZnO/NiO:rGO	hydrothermal	622.3 F g ⁻¹ at 1 A g ⁻¹	54.4% at 5 A g ⁻¹	[46]
Co(OH) ₂ @Ni(OH) ₂	electrodeposition	355.2 C g ⁻¹ at 1 A g ⁻¹	65.9% at 17 A g ⁻¹	[7]
Mn/Ni-MOF	solvothermal	793.6 F g ⁻¹ at 1 A g ⁻¹	51.9% at 20 A g ⁻¹	[47]

Zn-doped NiCo ₂ O ₄	hydrothermal	1499.0 F g ⁻¹ at 0.5 A g ⁻¹	66.7% at 10 A g ⁻¹	[48]
Zn/Ni-MOF	hydrothermal	878.0 F g ⁻¹ at 1 A g ⁻¹	61.0% at 10 A g ⁻¹	[49]
ZnO/NiO MOF	solvothermal	435.1 F g ⁻¹ at 1 A g ⁻¹	69.3% at 10 A g ⁻¹	[50]
ZNC-8.4%	colloidal method	750.5 C g⁻¹ at 0.5 A g⁻¹	72.9% at 10 A g⁻¹	This work

1 Fig. 3f represents the corresponding Nyquist plots of the ZN and ZNC-8.4%
2 electrodes in the frequency range of 0.01 Hz ~ 100 kHz with an amplitude of 5 mV. The
3 EIS curves are consisted of a semicircle in the high frequency region and a linear section
4 in the low frequency region [51]. At the high frequency region, the intercept between
5 the semicircle and the real axis (Z') replicates the internal resistance (R_s) of the
6 electrode, and the diameter of the semicircle represents the charge transfer resistance
7 (R_{ct}) of the electrode. At the low frequency region, the slope of the straight line reveals
8 the Warburg resistance (R_w) of the electrolyte diffusion, which is attributed to the ion
9 diffusion/transport of the electrolytes into the electrode [52]. The pseudo-capacitance-
10 type shows a small semicircle followed by a straight line of 90°, while the battery-type
11 shows a larger semicircle followed by a straight line of nearly 45° [54].

12 In Fig. 3f, the EIS image shows a large semicircle and a straight line close to 45°,
13 confirming that it is a battery-type material. The R_s and R_{ct} values of ZNC-8.4%
14 electrode are 0.89 Ω and 3.92 Ω , respectively. Compared with those of ZN electrode
15 ($R_s=0.88 \Omega$, $R_{ct}=4.34 \Omega$), the ZNC-8.4% electrode has a smaller value of R_{ct} and less
16 significantly changed internal resistance, indicating that the addition of CNTs can
17 effectively reduce the charge transfer resistance.

18 **3.3 Electrochemical performance of ZNC-8.4% //AC HSC**

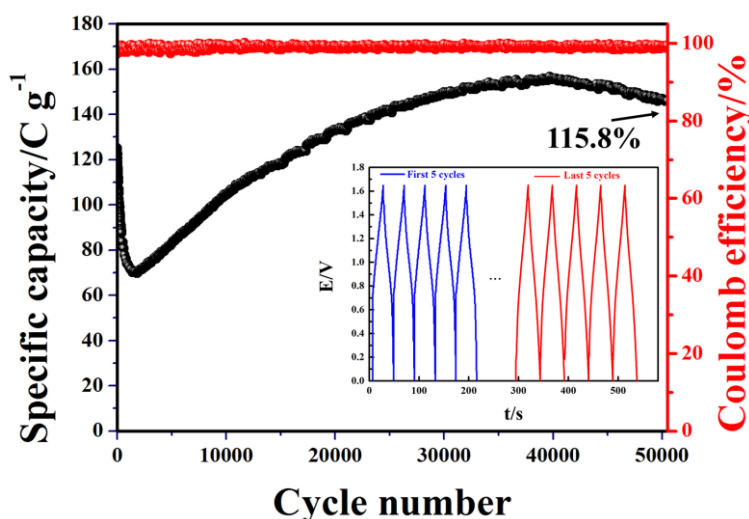


1

2 Fig. 4 (a) CV curves of ZNC-8.4% and AC at 10 mV s^{-1} , (b) CV curves at 10 mV s^{-1}
 3 and (c) GCD curves at 1 A g^{-1} of ZNC-8.4%/AC HSC at various voltage range, (d)
 4 CV curves of ZNC-8.4%/AC HSC at various scan rates, (e) GCD curves and (f)
 5 corresponding specific capacity values of the ZNC-8.4%/AC HSC at various current
 6 densities in 2 M KOH solution.

7 To further study the performance of ZNC-8.4% electrode, a ZNC-8.4%/AC hybrid
 8 supercapacitor (HSC) was assembled with the ZNC-8.4% electrode as positive
 9 electrode and the AC electrode as negative electrode. The CV curves of ZNC-8.4% and
 10 AC at the scan rate of 10 mV s^{-1} are shown in Fig. 4a. The obtained maximum potential
 11 of ASC device is 1.75 V. The CV and GCD curves of ZNC-8.4%/AC HSC devices
 12 under different potential ranges are shown in Figs. 4b and 4c. It is obvious that
 13 polarization has occurred when the potential reaches 1.65 V, and the range of the
 14 optimal potential window of HSC device is 0~1.65 V. Fig. 4d displays the CV curves
 15 of the HSC device at different scanning rates. The obtained CV curves at the scanning
 16 rates from 5 to 50 mV s^{-1} maintain stable shapes without apparent distortion, which

1 shows that the ZNC-8.4%/AC HSC has a good reversibility. Fig. 4e exhibits the GCD
 2 curves of the ZNC-8.4%/AC HSC at different current densities ranging from 0.5 to 10
 3 A g⁻¹. All the GCD curves shows good symmetrical triangle shapes, indicating the
 4 capacitive characteristics of the ZNC-8.4%/AC HSC. As shown in Fig. 4f, the
 5 corresponding specific capacity values of the ZNC-8.4%/AC HSC calculated based on
 6 GCD curves using equation (2) are 224.1, 201.7, 180.6, 161.5, 151.2, 142.4 and 135.0
 7 C g⁻¹ at various current densities of 0.5, 1, 2, 4, 6, 8, 10 A g⁻¹, respectively.

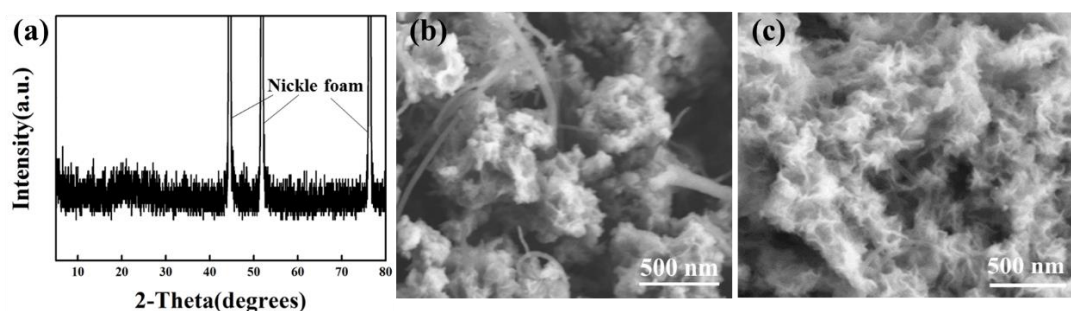


8
 9 Fig.5 Cycle performance of ZNC-8.4%/AC HSC at 6 A/g (inset: GCD curves of first
 10 and last 5 cycles).

11 Long-term cycling stability tests of ZNC-8.4%/AC HSC was conducted at 6 A/g and
 12 the obtained results are shown in Fig. 5. At the initial stage, the capacity of the ZNC-
 13 8.4%/AC HSC decreases and reaches its minimum at about 2,500 cycles. This is
 14 mainly because the structure of ZNC-8.4% was damaged during the charge/discharge
 15 processes, probably related to wettability issues [27]. After this stage, the structure was
 16 reassembled and the wettability between the surface of electrode and electrolyte was
 17 increased, which caused the increase of capacity [12]. After 50,000 cycles, the capacity

1 reaches 115.8% of the original value, and has a very good Coulomb efficiency of 99.4%.

2 ***3.4 Electrochemical performance of ZNC-8.4%//AC HSC after 50,000*** 3 ***cycles***

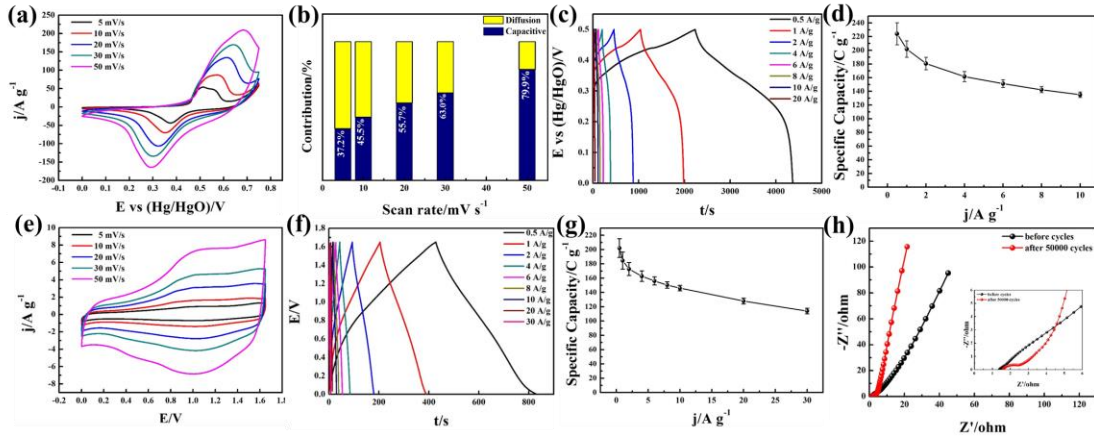


4

5 Fig. 6 (a) XRD spectrum of ZNC-8.4% after 50000 cycles, SEM images of ZNC-
6 8.4% (b) before 50,000 cycles and (c) after 50,000 cycles.

7 The electrochemical performance of ZNC-8.4%//AC HSC after long-term cycling
8 stability tests have been performed by testing the ZNC-8.4% electrode for ~50,000
9 cycles. XRD analysis (see in Fig. 6a) shows that there are no obvious diffraction peaks
10 other than those of nickel foam, indicating that the $\alpha\text{-Ni(OH)}_2\cdot 0.75\text{H}_2\text{O}$ crystalline
11 structure becomes amorphous after 50,000 cycles. Figs. 6b and 6c shows the SEM
12 images of the active electrode before and after 50,000 cycles. Before cycling process,
13 the sample shows a stacked flower-like clusters structure with nanosheets. Whereas
14 after 50,000 cycles, the nanosheets become much clearer and the flower-like structures
15 are stretched. These structural changes are kinetically controlled, which generally occur
16 during nucleation and growth processes [55]. This can increase specific surface areas
17 and provide more active sites for full contact with the electrolyte, thus showing good
18 electrochemical performance. The changes of crystalline structures and morphology of
19 ZNC-8.4% samples after 50,000 cycles lead to the decreases of the capacity firstly, but

1 then increases during the charge/discharge processes.



2

3 Fig. 7 (a) CV curves at the scan rate of 10 mV s⁻¹, (b) the contribution of diffusion and
 4 capacitive at different scan rate, (c) GCD curves from 0 to 0.5 V at different current
 5 density, (d) specific capacity for ZNC-8.4% electrode after 50,000 cycles tested in
 6 three electrode system, (e) CV curves and (f) GCD curves from 0 to 1.65 V, (g)
 7 specific capacitance and (h) Nyquist plots for the ZNC-8.4%//AC HSC after 50,000
 8 cycles. All electrochemical tests in 2 M KOH electrolyte.

9 The three-electrode test of the ZNC-8.4% electrode and the test of ZNC-8.4%//AC
 10 HSC after 50,000 cycles were further conducted and the obtained results are shown in
 11 Fig. 7. From the obtained CV curves shown in Fig. 7a, the ZNC-8.4% electrode has two
 12 obvious redox peaks after 50,000 cycles, showing its battery-type behavior. Fig. S6
 13 shows the calculated b value, which is 0.62 after the 50,000 cycles. Compared with that
 14 before the cycles (b=0.44), the b value is significantly increased, indicating that surface-
 15 controlled capacitance behavior plays a dominant role. The ratio between surface-
 16 controlled capacitance and diffusion-controlled battery-type behavior can be calculated
 17 based on the formulas [56-58]:

18

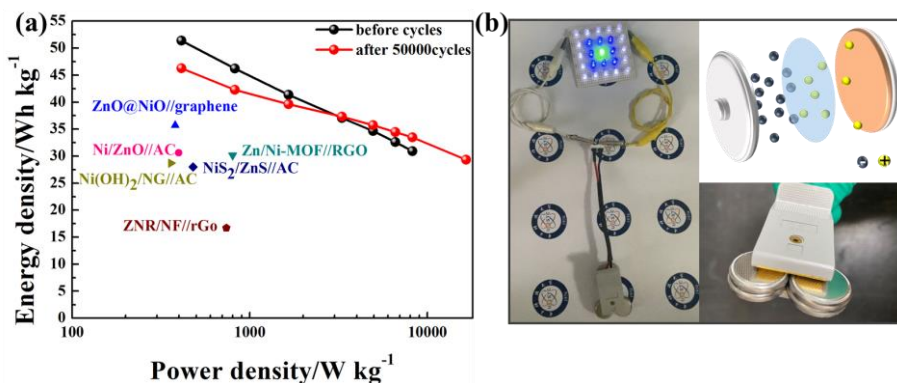
$$i(V) = k_1 v + k_2 v^{1/2} \quad (7)$$

1
$$i(V)/v^{1/2} = k_1v^{1/2} + k_2 \quad (8)$$

2 where i (V) and v (mV s^{-1}) are corresponding to the current density and sweep rate,
3 respectively. The total capacitance is composed of the surface-controlled one and
4 diffusion-controlled ones. By a linear fitting of $i/v^{1/2}$ and $v^{1/2}$, the value of k_1 and
5 k_2 can be obtained. Therefore, these capacitance contributions at different scanning
6 rates can be determined. As the scanning rate increases, the capacitance proportion is
7 gradually increased, and the capacitance contribution reaches 79.9% of its original
8 value at 50 mV s^{-1} from 37.2% at 5 mV s^{-1} (see in Fig. 7b). This is mainly because the
9 diffusion-controlled process is relatively slow, and much longer time is needed for
10 intercalation and migration of ions at a low scanning rate. However, for the surface-
11 controlled one, its reaction is mainly concentrated on the surface of electrode material,
12 thus it can respond much faster even at higher scanning rates [20]. Based on the data of
13 GCD curves of ZNC-8.4% electrode shown in Fig. 7c, the calculated specific capacity
14 values after 50,000 cycles are shown in Fig. 7d. The specific capacity value is 944.8 C
15 g^{-1} at the current density of 1 A g^{-1} , which is 130.0% of the previous value.

16 After 50,000 cycles, the ZNC-8.4%/AC HSC was tested with the optimal voltage
17 window of 1~1.65 V again. The obtained results are shown in Figs. S7a and S7b. In Fig.
18 7e, all the CV curves at different scanning rates show a rectangle-like shape with redox
19 peaks and no obvious changes in curve shapes with the increase of scan rate. Fig. 7f
20 shows the GCD curves of HSC, and the symmetry of the shape indicates good
21 reversibility. The specific capacities of ZNC-8.4%/AC after 50,000 cycles are 201.9,
22 184.5, 172.8, 162.7, 156.0, 150.4, 146.0, 128.0 and 114.0 C g^{-1} at current densities

1 ranging from 0.5 to 30 A g⁻¹, respectively (see in Fig. 7g). Therefore, the capacity of
 2 ZNC-8.4%//AC HSC maintains a good retention rate, e.g., a value of 61.7% at 30 A g⁻¹.
 3 Fig. 7h displays the EIS test results before and after the ZNC-8.4%//AC HSC cycles.
 4 It can be observed that the EIS curve after the cycles has a smaller semicircle and a
 5 larger slope than those before the cycle. Through resistance fitting, R_s is slightly
 6 increased to 1.6 Ω after 50,000 cycles from 1.4 Ω. However, the R_{ct} value of 0.9 Ω is
 7 much smaller than that before cycles (6.9 Ω). These results show that the electrode
 8 displays a better capacitive value after a long charge-discharge cycles.



9
 10 Fig. 8 (a) Ragone plots of ZNC-8.4%//AC HSC and other previously reported SCs,
 11 (b) photo of a LED bulb lit up by the ZNC-8.4%//AC HSC.

12 The energy density and power density of HSC were calculated according to the
 13 formulae (3) and (4), and the results are shown in Fig. 8a. Before the cycling, the energy
 14 density of ZNC-8.4%//AC HSC is 51.3 Wh kg⁻¹ at the power density is 409.6 W kg⁻¹.
 15 After 50,000 cycles, the maximum energy density of the HSC remains 46.2 Wh kg⁻¹.
 16 At a high power density of 16.5 kW kg⁻¹, it becomes 29.33 Wh kg⁻¹. Furthermore, the
 17 ZNC-8.4%//AC has both a larger energy density and a larger power density, when
 18 compared with those of the nickel based nanomaterials reported in literature, such as

1 Ni/ZnO//AC (30.6 Wh kg⁻¹ at 398 W kg⁻¹) [17], ZnO/NiO:rGO//rGO (16.7 Wh kg⁻¹ at
2 737.6 W kg⁻¹) [46], Zn/Ni-MOF//RGO (30.5 Wh kg⁻¹ at 800 W kg⁻¹) [49], Ni(OH)₂/
3 Nitrogen-enriched graphene //AC (28.7 Wh kg⁻¹ at 360 W kg⁻¹) [44], NiS₂/ZnS//AC
4 (28.0 Wh kg⁻¹ at 478.9 W kg⁻¹) [57] and ZnO@NiO// graphene (35.7 Wh kg⁻¹ at 380.9
5 W kg⁻¹) [51]. Therefore, the ZNC-8.4%//AC HSC prepared in this work shows excellent
6 performance as energy storage device. For a demonstration, Fig. 8b shows a photo in
7 which a LED bulb has been effectively lit up using the ZNC-8.4%//AC HSC.

8

9 **4 Conclusions**

10 The flower-like Zn doped Ni(OH)₂@CNTs with excellent electrochemical
11 performance were directly synthesized by the colloidal method at room temperature.
12 The specific capacity of the ZNC-8.4% electrode reaches 726.5 C g⁻¹ when the current
13 density is 1 A g⁻¹, and remains 72.9% of its original value at 10 A g⁻¹. The assembled
14 ZNC-8.4%//AC HSC can achieve a high energy density of 51.3 Wh kg⁻¹ at the power
15 density of 409.6 W kg⁻¹. After 50,000 cycles, the ZNC-8.4% shows an increased
16 specific capacity of 944.8 C g⁻¹ at 1 A g⁻¹. Moreover, the energy density of ZNC-
17 8.4%//AC HSC can still keep 29.33 Wh kg⁻¹ at the high power density of 16.5 kW kg⁻¹.
18 Therefore, ZNC-8.4% has a promising practical application as energy storage electrode
19 materials.

20

21 **Acknowledgements**

22 The authors would like to acknowledge International Exchange Grant

1 (IEC/NSFC/201078) through Royal Society and National Science Foundation of China
2 (NSFC).

3

4 **Reference**

5 [1] J. Acharya, T.H. Ko, M.K. Seo, M.S. Khil, H. Y. Kim, B.S. Kim, Engineering the
6 hierarchical heterostructures of Zn-Ni-Co nanoneedles arrays@Co-Ni-LDH nanosheets
7 core-sheath electrodes for a hybrid asymmetric supercapacitor with high energy density
8 and excellent cyclic stability, ACS Appl. Energy Mater. 3 (2020) 7383-7396.

9 [2] H. Li, Z. Li, M. Sun, Z. Wu, W. Shen, Y. Fu, Zinc cobalt sulfide nanoparticles as
10 high performance electrode material for asymmetric supercapacitor, Electrochim. Acta
11 319 (2019) 716-726.

12 [3] A. Elgendy, N.M. El Basiony, F.E.T. Heikal, A.E. Elkholy, Mesoporous Ni-Zn-Fe
13 layered double hydroxide as an efficient binder-free electrode active material for high-
14 performance supercapacitors, J. Power Sources 466 (2020) 228294.

15 [4] S. Li, Y. Zhang, N. Liu, C. Yu, S.J. Lee, S. Zhou, R. Fu, J. Yang, W. Guo, H. Huang,
16 J.-S. Lee, C. Wang, T.R. Kim, D. Nordlund, P. Pianetta, X. Du, J. Zhao, Y. Liu, J. Qiu,
17 Operando revealing dynamic reconstruction of NiCo carbonate hydroxide for high-rate
18 energy storage, Joule 4 (2020) 673-687.

19 [5] B. Kirubasankar, P. Palanisamy, S. Arunachalam, V. Murugadoss, S. Angaiah, 2D
20 MoSe₂-Ni(OH)₂ nanohybrid as an efficient electrode material with high rate capability
21 for asymmetric supercapacitor applications, Chem. Eng. J. 355 (2019) 881-890.

22 [6] X. Chen, S. Wang, G. Qiao, X. Wang, G. Lu, H. Cui, X. Wang, Sepiolite/amorphous

1 nickel hydroxide hierarchical structure for high capacitive supercapacitor, *J. Alloy.*
2 *Compd.* 881 (2021) 160519.

3 [7] A. Sharifi, M. Arvand, S. Daneshvar, A novel flexible wire-shaped supercapacitor
4 with enhanced electrochemical performance based on hierarchical $\text{Co}(\text{OH})_2@ \text{Ni}(\text{OH})_2$
5 decorated porous dendritic Ni film/Ni wire, *J. Alloy. Compd.* 856 (2021) 158101.

6 [8] J. Cao, Q. Mei, R. Wu, W. Wang, Flower-like nickel-cobalt layered hydroxide
7 nanostructures for super long-life asymmetrical supercapacitors, *Electrochim. Acta* 321
8 (2019) 134711.

9 [9] S. Yang, C. Wu, J. Cai, Y. Zhu, H. Zhang, Y. Lu, K. Zhang, Seed-assisted smart
10 construction of high mass loading Ni-Co-Mn hydroxide nanoflakes for supercapacitor
11 applications, *J. Mater. Chem. A* 5 (2017) 16776-16785.

12 [10] L. Zhang, Z. Xiong, X.S. Zhao, A composite electrode consisting of nickel
13 hydroxide, carbon nanotubes, and reduced graphene oxide with an ultrahigh
14 electrocapacitance, *J. Power Sources* 222 (2013) 326-332.

15 [11] D. Wang, B. Guan, Y. Li, D. Li, Z. Xu, Y. Hu, Y. Wang, H. Zhang, Morphology-
16 controlled synthesis of hierarchical mesoporous $\alpha\text{-Ni}(\text{OH})_2$ microspheres for high-
17 performance asymmetric supercapacitors, *J. Alloy. Compd.* 737 (2018) 238-247.

18 [12] J. Yan, Z. Fan, W. Sun, G. Ning, T. Wei, Q. Zhang, R. Zhang, L. Zhi, F. Wei,
19 Advanced asymmetric supercapacitors based on $\text{Ni}(\text{OH})_2/\text{Graphene}$ and porous
20 graphene electrodes with high energy density, *Adv. Funct. Mater.* 22 (2012) 2632-2641.

21 [13] J. Yang, C. Zheng, P. Xiong, Y. Li, M. Wei, Zn-doped Ni-MOF material with a
22 high supercapacitive performance, *J. Mater. Chem. A* 2 (2014) 19005-19010.

- 1 [14] X. Guan, M. Huang, L. Yang, G. Wang, X. Guan, Facial design and synthesis of
2 $\text{CoS}_x/\text{Ni-Co}$ LDH nanocages with rhombic dodecahedral structure for high-
3 performance asymmetric supercapacitors, *Chem. Eng. J.* 372 (2019) 151-162.
- 4 [15] G. Manibalan, Y. Govindaraj, J. Yesuraj, P. Kuppusami, G. Murugadoss, R.
5 Murugavel, M. Rajesh Kumar, Facile synthesis of $\text{NiO}@\text{Ni}(\text{OH})_2\text{-}\alpha\text{-MoO}_3$
6 nanocomposite for enhanced solid-state symmetric supercapacitor application, *J.*
7 *Colloid. Interf. Sci.* 585 (2021) 505-518.
- 8 [16] I. Hussain, T. Hussain, S. Yang, Y. Chen, J. Zhou, X. Ma, N. Abbas, C. Lamiel, K.
9 Zhang, Integration of CuO nanosheets to Zn-Ni-Co oxide nanowire arrays for energy
10 storage applications, *Chem. Eng. J.* 413 (2021) 127570.
- 11 [17] A. Tang, C. Wan, X. Hu, X. Ju, Metal-organic framework-derived Ni/ZnO nano-
12 sponges with delicate surface vacancies as anode materials for high-performance
13 supercapacitors, *Nano Res.* 857 (2021) 58275.
- 14 [18] Z. Zhang, H. Huo, Z. Yu, L. Xiang, B. Xie, C. Du, J. Wang, G. Yin, Unraveling the
15 reaction mechanism of low dose Mn dopant in $\text{Ni}(\text{OH})_2$ supercapacitor electrode, *J.*
16 *Energy Chem.* 61 (2021) 497-506.
- 17 [19] A.V. Radhamani, M. Krishna Surendra, M.S.R. Rao, Zn doped $\delta\text{-MnO}_2$ nano flakes:
18 An efficient electrode material for aqueous and solid state asymmetric supercapacitors,
19 *Appl. Surf. Sci.* 450 (2018) 209-218.
- 20 [20] Y. Du, G. Li, L. Ye, C. Che, X. Yang, L. Zhao, Sandwich-like Ni-Zn hydroxide
21 nanosheets vertically aligned on reduced graphene oxide via MOF templates towards
22 boosting supercapacitive performance, *Chem. Eng. J.* 417 (2021) 129189.

- 1 [21] H. Wu, X. Zhang, J. Xue, H. Zhang, L. Yang, S. Li, Engineering active sites on
2 hierarchical ZnNi layered double hydroxide architectures with rich Zn vacancies
3 boosting battery-type supercapacitor performances, *Electrochim. Acta* 374 (2021)
4 137932.
- 5 [22] G. Li, M. Chen, Y. Ouyang, D. Yao, L. Lu, L. Wang, X. Xia, W. Lei, S.-M. Chen,
6 D. Mandler, Q. Hao, Manganese doped Co_3O_4 mesoporous nanoneedle array for long
7 cycle-stable supercapacitors, *Appl. Surf. Sci.* 469 (2019) 941-950.
- 8 [23] H. Jiang, P.S. Lee, C. Li, 3D carbon based nanostructures for advanced
9 supercapacitors, *Energy Environ. Sci.* 6 (2013) 41-53.
- 10 [24] H. Li, Z. Li, Z. Wu, M. Sun, S. Han, C. Cai, W. Shen, X. Liu, Y. Fu, Enhanced
11 electrochemical performance of CuCo_2S_4 /carbon nanotubes composite as electrode
12 material for supercapacitors, *J Colloid. Interf. Sci.* 549 (2019) 105-113.
- 13 [25] M. Sun, Z. Li, H. Li, Z. Wu, W. Shen, Y.Q. Fu, Mesoporous Zr-doped CeO_2
14 nanostructures as superior supercapacitor electrode with significantly enhanced specific
15 capacity and excellent cycling stability, *Electrochim. Acta* 331 (2020) 135366.
- 16 [26] M. Sun, Z. Li, Q. Fang, S. Han, C. Cai, H. Li, W. Shen, X. Liu, Y. Fu, Room-
17 temperature synthesized porous $\text{Cu}(\text{OH})_2/\text{Cu}_7\text{S}_4$ hybrid nanowires as a high-
18 performance electrode material for asymmetric supercapacitors, *J. Mater. Chem. A* 8
19 (2020) 724-734.
- 20 [27] L. Zhu, C. Hao, X. Wang, Y. Guo, Fluffy Cotton-like GO/Zn-Co-Ni layered double
21 hydroxides form from a sacrificed template GO/ZIF-8 for high performance
22 asymmetric supercapacitors, *ACS Sustain. Chem. Eng.* 8 (2020) 11618-11629.

- 1 [28] Y. Zhu, C. Huang, C. Li, M. Fan, K. Shu, H.C. Chen, Strong synergetic
2 electrochemistry between transition metals of α phase Ni-Co-Mn hydroxide contributed
3 superior performance for hybrid supercapacitors, *J. Power Sources* 412 (2019) 559-567.
- 4 [29] B. Zhao, L. Zhang, Q. Zhang, D. Chen, Y. Cheng, X. Deng, Y. Chen, R. Murphy,
5 X. Xiong, B. Song, C.P. Wong, M.S. Wang, M. Liu, Rational design of nickel
6 hydroxide-based nanocrystals on graphene for ultrafast energy storage, *Adv. Energy*
7 *Mater.* 8 (2018) 1702247.
- 8 [30] Y. Chen, D. Ni, X. Yang, C. Liu, J. Yin, K. Cai, Microwave-assisted synthesis of
9 honeycomblike hierarchical spherical Zn-doped Ni-MOF as a high-performance
10 battery-type supercapacitor electrode material, *Electrochim. Acta* 278 (2018) 114-123.
- 11 [31] J.Y. Lee, K. Liang, K.H. An, Y.H. Lee, Nickel oxide/carbon nanotubes
12 nanocomposite for electrochemical capacitance, *Synthetic Met.* 150 (2005) 153-157.
- 13 [32] X. Ma, Z. Kang, A facile electrodeposition technique for synthesis of nickel
14 sulfides/carbon nanotubes nanocomposites as high performance electrodes for
15 supercapacitor, *Mater. Lett.* 236 (2019) 468-471.
- 16 [33] E. Baasanjav, P. Bandyopadhyay, G. Saeed, S. Lim, S.M. Jeong, Dual-ligand
17 modulation approach for improving supercapacitive performance of hierarchical zinc-
18 nickel-iron phosphide nanosheet-based electrode, *J. Ind. Eng. Chem.* 99 (2021) 299-
19 308.
- 20 [34] G. Saeed, P. Bandyopadhyay, S. Kumar, N.H. Kim, J.H. Lee, ZnS-Ni₇S₆ nanosheet
21 arrays wrapped with nanopetals of Ni(OH)₂ as a novel core-shell electrode material for
22 asymmetric supercapacitors with high energy density and cycling stability performance,

- 1 ACS Appl. Mater. Inter. 12 (2020) 47377-47388.
- 2 [35] A. Ali, I. Hameed, M. Ammar, R. Mujahid, S. Mirza, Enhanced rate capability for
3 asymmetric supercapacitors by binder-free Zn-Ni-Co oxide nanoflakes on Ni foam, J.
4 Energy Storage 37 (2021) 102472.
- 5 [36] P. Bandyopadhyay, G. Saeed, N. Hoon Kim, S. Mun Jeong, J. Hee Lee, Fabrication
6 of hierarchical Zn-Ni-Co-S nanowire arrays and graphitic carbon nitride/graphene for
7 solid-state asymmetric supercapacitors, Appl. Surf. Sci. 542 (2021) 148564.
- 8 [37] Y. Zou, C. Cai, C. Xiang, P. Huang, H. Chu, Z. She, F. Xu, L. Sun, H.-B. Kraatz,
9 Simple synthesis of core-shell structure of Co-Co₃O₄@carbon-nanotube-incorporated
10 nitrogen-doped carbon for high-performance supercapacitor, Electrochim. Acta 261
11 (2018) 537-547.
- 12 [38] X. Liu, C. Liu, H. Wan, J. Zhang, P. Liang, H. Wang, H. Wang, Ultra-long life
13 nickel nanowires@nickel-cobalt hydroxide nanoarrays composite pseudocapacitive
14 electrode: Construction and activation mechanism, Electrochim. Acta 259 (2018) 303-
15 312.
- 16 [39] P. Sharma, M.M. Sundaram, T. Watcharatharapong, D. Laird, H. Euchner, R. Ahuja,
17 Zn metal atom doping on the surface plane of one-dimensional NiMoO₄ nanorods with
18 improved redox chemistry, ACS Appl. Mater. Inter. 12 (2020) 44815-44829.
- 19 [40] M. Li, L. Fang, H. Zhou, F. Wu, Y. Lu, H. Luo, Y. Zhang, B. Hu, Three-dimensional
20 porous MXene/NiCo-LDH composite for high performance non-enzymatic glucose
21 sensor, Appl. Surf. Sci. 495 (2019) 143554.
- 22 [41] H. Hosseini, S. Shahrokhian, Self-supported nanoporous Zn-Ni-Co/Cu selenides

1 microball arrays for hybrid energy storage and electrocatalytic water/urea splitting,
2 Chem. Eng. J. 375 (2019).

3 [42] S. Zhang, Y. Pang, Y. Wang, B. Dong, S. Lu, M. Li, S. Ding, NiO nanosheets
4 anchored on honeycomb porous carbon derived from wheat husk for symmetric
5 supercapacitor with high performance, J. Alloy. Compd. 735 (2018) 1722-1729.

6 [43] J. Li, H. Hao, J. Wang, W. Li, W. Shen, Hydrogels that couple nitrogen-enriched
7 graphene with Ni(OH)₂ nanosheets for high-performance asymmetric supercapacitors,
8 J. Alloy. Compd. 782 (2019) 516-524.

9 [44] X. Jiang, S. Deng, L. Sun, J. Liu, N. Qi, Z. Chen, Pillared nickel-based metal-
10 organic frameworks as electrode material with high electrochemical performance, J.
11 Electroanal. Chem. 879 (2020) 114802.

12 [45] S. Arunpandiyan, A. Raja, S. Bharathi, A. Arivarasan, Fabrication of ZnO/NiO:
13 rGO coated Ni foam binder-free electrode via hydrothermal method for supercapacitor
14 application, J. Alloy. Compd. 883 (2021) 160791.

15 [46] Y. Han, J. Zhou, L. Wang, L. Xing, Z. Xue, Y. Jiao, Y. Pang, Redox-active
16 nanostructure electrode of Mn/Ni bimetal organic frameworks anchoring on multi-
17 walled carbon nanotubes for advanced supercapacitor, J. Electroanal. Chem. 882 (2021)
18 114993.

19 [47] K. Gao, S.-D. Li, Hollow fibrous NiCo₂O₄ electrodes with controllable Zn
20 substitution sites for supercapacitors, J. Alloy. Compd. 832 (2020) 154927.

21 [48] X. Zhang, Y. Sui, F. Wei, J. Qi, Q. Meng, Y. Ren, Y. He, Self-supported 3D layered
22 zinc/nickel metal-organic-framework with enhanced performance for supercapacitors,

- 1 J. Mater. Sci-Mater. El. 30 (2019) 18101-18110.
- 2 [49] P. Yang, X. Song, C. Jia, H.-S. Chen, Metal-organic framework-derived
3 hierarchical ZnO/NiO composites: Morphology, microstructure and electrochemical
4 performance, J. Ind. Eng. Chem. 62 (2018) 250-257.
- 5 [50] Y. Ouyang, X. Xia, H. Ye, L. Wang, X. Jiao, W. Lei, Q. Hao, Three-dimensional
6 hierarchical structure ZnO@C@NiO on carbon cloth for asymmetric supercapacitor
7 with enhanced cycle stability, ACS Appl. Mater. Inter. 10 (2018) 3549-3561.
- 8 [51] H. Li, Z. Li, Z. Wu, M. Sun, S. Han, C. Cai, W. Shen, Y. Fu, Nanocomposites of
9 cobalt sulfide embedded carbon nanotubes with enhanced supercapacitor performance,
10 J. Electrochem. Soc. 166 (6) (2019) A1031-A1037.
- 11 [52] Y. Zhou, Z. Jia, Y. Shen, L. Wei, S. Zhao, Y. Han, P. Chen, C. Xu, X. Cui, J. Sun,
12 X. Ouyang, X. Wang, J. Zhu, S. Pan, Y. Fu, Ingenious construction of hierarchical
13 spherical nanostructures by in-situ confining Ni-Co-Mn hydroxide nanosheets
14 inside/outside hollow carbon nanospheres for high-performance hybrid supercapacitors,
15 J. Energy Storage 36 (2021) 102380.
- 16 [53] M. Sun, Q. Fang, Z. Li, C. Cai, H. Li, B. Cao, W. Shen, T.X. Liu, Y. Fu, Co-
17 precipitation synthesis of CuCo_2O_4 nanoparticles for supercapacitor electrodes with
18 large specific capacity and high rate capability, Electrochim. Acta 397 (2021) 139306.
- 19 [54] Q. Fang, M. Sun, X. Ren, B. Cao, W. Shen, Z. Li, Y. Fu, Ultrafine Mn_3O_4 nanowires
20 synthesized by colloidal method as electrode materials for supercapacitors with a wide
21 voltage range, J. Energy Storage 44 (2021) 103260.
- 22 [55] H. Hosseini, S. Shahrokhian, Vanadium dioxide-anchored porous carbon

1 nanofibers as a Na⁺ intercalation pseudocapacitance material for development of
2 flexible and super light electrochemical energy storage systems, *Appl. Mater. Today* 10
3 (2018) 72-85.

4 [56] L. Ye, Y. Zhou, Z. Bao, Y. Zhao, Y. Zou, L. Zhao, Q. Jiang, Sheet-membrane Mn-
5 doped nickel hydroxide encapsulated via heterogeneous Ni₃S₂ nanoparticles for
6 efficient alkaline battery-supercapacitor hybrid devices, *J. Mater. Chem. A* 6 (2018)
7 19020-19029.

8 [57] G.C. Li, M. Liu, M.K. Wu, P.F. Liu, Z. Zhou, S.-R. Zhu, R. Liu, L. Han, MOF-
9 derived self-sacrificing route to hollow NiS₂/ZnS nanospheres for high performance
10 supercapacitors, *RSC Adv.* 6 (2016) 103517-103522.

11 [58] Y. Zhou, Z. Jia, S. Zhao, Y. Wang, T. Guo, L. Wei, X. Cui, X. Ouoyang, X. Wang,
12 J. Zhu, J. Sun, S. Pan, Construction of triple-shelled hollow nanostructure by confining
13 amorphous Ni-Co-S/crystalline MnS on/in hollow carbon nanospheres for all-solid-
14 state hybrid supercapacitors, *Chem. Eng. J.* 416 (2021) 129500.